

# Supplemental material: Mode selection in compressible active flow networks

Aden Forrow,<sup>1</sup> Francis G. Woodhouse,<sup>2</sup> and Jörn Dunkel<sup>1</sup>

<sup>1</sup>*Department of Mathematics, Massachusetts Institute of Technology,  
77 Massachusetts Avenue, Cambridge MA 02139-4307, U.S.A.*

<sup>2</sup>*Department of Applied Mathematics and Theoretical Physics, Centre for Mathematical Sciences,  
University of Cambridge, Wilberforce Road, Cambridge CB3 0WA, U.K.*

## I. NONDIMENSIONALIZATION OF GOVERNING EQUATIONS

We can define the model in terms of the dimensional quantities  $\hat{\varrho}_v$ ,  $\hat{\phi}_e$ , and  $\hat{t}$ ; global dimensional parameters  $\hat{\epsilon}$ ,  $\hat{\beta}$ , and  $\hat{D}$ ; dimensionless edge conductances  $\gamma_e$  and vertex volumes  $m_v$ ; and a dimensionless global parameter  $\mu$  and function  $g$  as

$$\begin{aligned}\frac{d\hat{\varrho}_v}{d\hat{t}} &= \sum_e \nabla_{ve} \hat{\phi}_e, \\ \frac{d\hat{\phi}_e}{d\hat{t}} &= -\hat{\gamma}_e \sum_v \nabla_{ev}^\top m_v^{-1} \hat{\varrho}_v + \hat{\epsilon} g\left(\mu, \frac{\hat{\phi}_e}{\hat{\beta} \hat{\gamma}_e}\right) \hat{\phi}_e + \sqrt{2\hat{D}} \hat{\xi}_e(\hat{t}).\end{aligned}$$

The scaling by conductance in the argument of  $g$  is chosen to match the phenomenology observed in dense bacterial suspensions, where activity selects a characteristic velocity  $\phi_e/\gamma_e$  and not a fixed flux  $\phi_e$ . If we choose a conductance scale  $\hat{\gamma}$  and volume scale  $\hat{m}$  and insert the rescaled, nondimensional parameters

$$\gamma_e = \hat{\gamma}^{-1} \hat{\gamma}_e, \quad m_v = \hat{m}^{-1} \hat{m}_v, \quad \epsilon = \hat{\gamma}^{-\frac{1}{2}} \hat{\epsilon}, \quad D_e = \hat{\beta}^{-2} \hat{\gamma}^{-\frac{1}{2}} \gamma_e^{-1} \hat{D}$$

and variables

$$\varrho_v = m_v^{\frac{1}{2}} \hat{\gamma}^{\frac{1}{2}} \hat{\beta}^{-1} \hat{\varrho}_v, \quad \phi_e = \gamma_e^{-\frac{1}{2}} \hat{\beta}^{-1} \hat{\phi}_e, \quad t = \hat{\gamma}^{\frac{1}{2}} \hat{t}, \quad \xi_e(t) = \hat{\gamma}^{-\frac{1}{4}} \hat{\xi}_e(\hat{t}),$$

we are left with

$$\begin{aligned}\frac{d\varrho_v}{dt} &= \sum_e m_v^{-1/2} \nabla_{ve} \gamma_e^{1/2} \phi_e, \\ \frac{d\phi_e}{dt} &= -\sum_v \gamma_e^{1/2} \nabla_{ev}^\top m_v^{-1/2} \varrho_v + \epsilon g\left(\mu, \frac{\phi_e}{\sqrt{\gamma_e}}\right) \phi_e + \sqrt{2D_e} \xi_e(t).\end{aligned}$$

With constant conductances  $\gamma_e = 1$  and volumes  $m_v = 1$ , we recover the model introduced in the main text, namely

$$\frac{d\varrho_v}{dt} = \sum_e \nabla_{ve} \phi_e, \tag{S1a}$$

$$\frac{d\phi_e}{dt} = -\sum_v \nabla_{ev}^\top \varrho_v + \epsilon g(\mu, \phi_e) \phi_e + \sqrt{2D_e} \xi_e(t), \tag{S1b}$$

with nonzero entries of the gradient matrix equal to  $\pm 1$ . All of our analysis applies equally well to the varying weights case: the only substantive change is replacing  $\nabla_{ve}$  with the weighted gradient  $\nabla_{ve}^* = m_v^{-1/2} \nabla_{ve} \gamma_e^{1/2}$ .

We can combine Eqs. (S1a) and (S1b) into one second order equation for the pressure dynamics reading

$$\ddot{\varrho}_v = \sum_e \nabla_{ve} \left( -\sum_u \nabla_{eu}^\top \varrho_u + \epsilon g(\mu, \phi_e) \phi_e + \sqrt{2D_e} \xi_e(t) \right). \tag{S2}$$

In the absence of friction, when  $g(\mu, \phi_e) = 0$ , the dynamics are Hamiltonian with energy

$$H = \frac{1}{2} \sum_{v,e,u} \varrho_v \nabla_{ve} \nabla_{eu}^\top \varrho_u + \frac{1}{2} \sum_{e,v,f} \phi_e \nabla_{ev}^\top \nabla_{vf} \phi_f. \tag{S3}$$

The energy is particularly simple when written in the basis of singular vectors of  $\nabla^\top$  with non-zero singular values, giving

$$H = \frac{1}{2} \sum_n \lambda_n^2 (r_n^2 + f_n^2) \equiv \sum_n H_n.$$

## II. RELATION TO PHYSICAL FLOW SYSTEMS

We chose to explore a minimal model coupling local active energy input to network structure, rather than capture the details of any particular model system. Nevertheless, the key features of our model, namely mass conservation and a polynomial expansion of the active term, are generic enough to be straightforwardly adapted to a range of applications.

Mass conservation and pressure driven flow are likely to remain in any active flow model; the form of the active term may change in different contexts. In our case, staying close to examples of bacterial suspensions, we model activity as driving spontaneous flow on all edges. An alternative option, more closely related to shuttle streaming in networks, would be to apply an active force  $f_v$  that compresses or expands each vertex and drives flow in or out, with modified dynamics

$$\begin{aligned}\frac{d\varrho_v}{dt} &= \sum_e \nabla_{ve} \phi_e, \\ \frac{d\phi_e}{dt} &= - \sum_v \nabla_{ev}^\top (\varrho_v + \epsilon f_v) + \sqrt{2D} \xi_e(t).\end{aligned}$$

The correct form of the active force depends on the microscopic details of the driving. Some generic features, however, will not depend on the exact form of  $f_v$  and will be discoverable by choosing a simple function of local quantities ( $\varrho_v, \dot{\varrho}_v$ , etc.) as an approximate driving force.

The same method is used to derive the Toner-Tu equations for continuous active flows [1]; our model can be understood as a discrete version of a special case of these equations. If advective and diffusive terms are rendered negligible in favor of pressure-driven and activity-driven flow by geometric effects or otherwise, and we take only the linear term in the virial expansion of the active pressure, the general Toner-Tu model simplifies to

$$\frac{\partial \vec{v}}{\partial t} = \alpha \vec{v} - \beta |\vec{v}|^2 \vec{v} - \sigma_1 \vec{\nabla}(\rho - \rho_0) + \vec{f}, \quad \frac{\partial \rho}{\partial t} + \vec{\nabla} \cdot (\vec{v} \rho) = 0.$$

In a limit where deviations from the mean density are small, so  $\rho = \rho_0 + \eta \varrho$  for some  $\eta \ll 1$ , we can further reduce to

$$\frac{\partial \vec{v}}{\partial t} = \alpha \vec{v} - \beta |\vec{v}|^2 \vec{v} - \eta \sigma_1 \vec{\nabla} \varrho + \vec{f}, \quad \eta \frac{\partial \varrho}{\partial t} + (\rho_0 + \eta \varrho) \vec{\nabla} \cdot \vec{v} + \eta \vec{v} \cdot \vec{\nabla} \varrho = 0.$$

Then on short time scales  $\tau = t/\eta$ , we have

$$\frac{\partial \vec{v}}{\partial \tau} = \eta \alpha \vec{v} - \eta \beta |\vec{v}|^2 \vec{v} - \eta^2 \sigma_1 \vec{\nabla} \varrho + \eta \vec{f}, \quad \frac{\partial \varrho}{\partial \tau} \approx -\rho_0 \vec{\nabla} \cdot \vec{v},$$

where we neglect terms that must be of order  $\eta$ : if the coefficients  $\alpha$ ,  $\beta$ , and  $\sigma_1$  are sufficiently large, their terms will remain relevant. The scaling of  $\tau$  ensures that  $t$  is small when  $\tau$  is order one or smaller. Discretizing the velocity and density fields as well as the noise  $\vec{f}$  and replacing the continuous gradient with either  $\nabla_{ev}^\top$  or  $-\nabla_{ve}$  as appropriate yields Eqs. (S1).

## III. COMPRESSIBILITY

Compressibility as included in our model is intended to describe changes in density or volume of the active component, not the underlying fluid. For example, variations in  $\varrho$  may be interpreted as variations in the density of swimmers in a bacterial system or variations in the tube volume in *Physarum polycephalum*. Such systems may be effectively compressible even though the solvent fluid (e.g. water) is incompressible.

In some cases, compressibility is the primary object of interest. For example, a recent preprint [2] discusses sound in active fluids in a network using a continuous wave equation derived from the Toner-Tu model. On top of a background flow taking the form of a lattice of counter-rotating cycles, they find modes confined to the edges of a Lieb lattice, which we can reproduce in our discretized setting (Fig. S1 and Movie 3). In both their setting and ours, these edge modes decay over time without propagating into the bulk (cf. discussion in App. I.B of Ref. [2]).

We can recover an incompressible limit of our model by first extending it to include damping on the vertices:

$$\frac{d\varrho_v}{dt} = \sum_e \nabla_{ve} \phi_e - \eta \varrho_v, \tag{S8a}$$

$$\frac{d\phi_e}{dt} = -\gamma \sum_v \nabla_{ev}^\top \varrho_v + \epsilon g(\mu, \phi_e) \phi_e + \sqrt{2D} \xi_e(t). \tag{S8b}$$

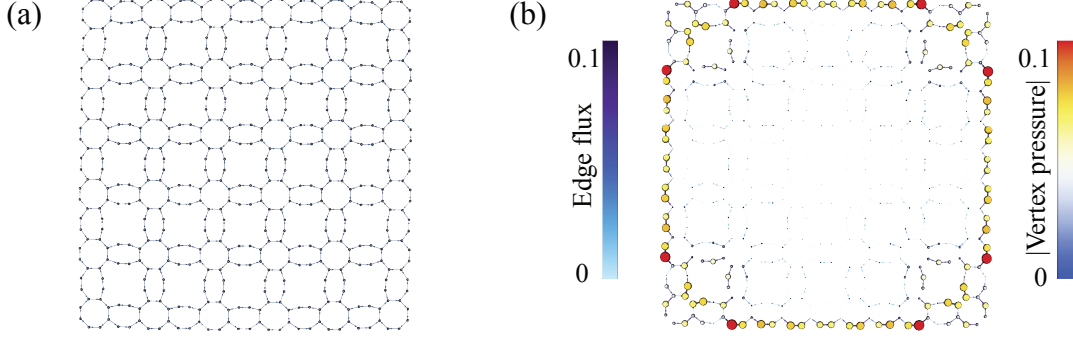


Fig. S1. Our active network model exhibits behavior similar to the topological edge modes of [2]. (a) A discretized version of the Lieb lattice considered in [2]. Edges shared by adjacent 8-cycles have weight  $\gamma_e = 2$  to account for the additional width of the corresponding channels. The most stable flow on this network consists of a lattice of counter-rotating cycles, in which both the active friction term  $g(\mu, \phi_e/\sqrt{\gamma_e})$  and the pressure variations  $\varrho_v$  are everywhere zero. (b) This lattice has modes confined to the edges of the domain, allowing sound waves to propagate and decay without scattering into the bulk (cf. discussion in App. I.B of Ref. [2]); one such mode is pictured. Simulations started in this mode as a perturbation to the most stable flow pattern do not cause density changes in the center (Movie 3). The network model allows study of such phenomena without resorting to full scale simulation of the flow patterns.

This paper examines the limit  $\eta \rightarrow 0$  where total mass is exactly conserved. Previous work [3] has looked at the opposite limit,  $\eta \rightarrow \infty$ , where Eq. (S8a) can only be balanced if  $\varrho_v \rightarrow 0$  and

$$\varrho_v = \frac{1}{\eta} \sum_e \nabla_{ve} \phi_e.$$

Substituting this into Eq. (S8b) gives

$$\frac{d\phi_e}{dt} = -\frac{\gamma}{\eta} \sum_v \nabla_{ev}^\top \nabla_{va} \phi_a + \epsilon g(\mu, \phi_e) \phi_e + \sqrt{2D} \xi_e(t).$$

With  $g(\mu, \phi_e) = \phi_e^2(1 - \phi_e^2)$ , this is equivalent to the model discussed in [3]. If  $\gamma \rightarrow \infty$  so that  $\gamma/\eta$  is constant, small deviations from incompressibility are allowed; if  $\gamma/\eta \rightarrow \infty$ , incompressibility is fully enforced. However, compressibility is a necessary ingredient for sound waves [2] and density oscillations [4].

#### IV. RAYLEIGH FRICTION APPROXIMATION

While choosing the friction function to be [5]

$$g(\mu, \phi_e) = \frac{\mu - \phi_e^2}{1 + \phi_e^2}$$

has convenient theoretical properties, namely that it gives a passive constant friction coefficient  $\epsilon$  for  $\mu = -1$  and for  $\phi \rightarrow \infty$ , it is analytically difficult. To simplify the analysis, we approximate this  $g(\mu, \phi_e)$  with a symmetric quadratic [6]

$$\hat{g}(\mu, \phi_e) = a - b\phi_e^2, \quad (\text{S9})$$

where  $a = \mu$  and  $b = 1$  are chosen so that  $\hat{g}(\mu, 0) = g(\mu, 0)$  and  $\hat{g}(\mu, \phi_e)$  has the same zeros as  $g(\mu, \phi_e)$ . This ensures that the two functions approximately match when they are both negative, that is, when activity is putting energy into the flow. The large difference between  $g(\mu, \phi_e)$  and  $\hat{g}(\mu, \phi_e)$  when the flux is large is less important, as the flow will be damped down in either case. The larger damping in  $\hat{g}(\mu, \phi_e)$  does result in slightly lower steady amplitudes, both analytically and in simulations.

## V. PERTURBATION EXPANSION

If  $\epsilon$  is small, there will be two widely separated timescales: the fast oscillation timescale  $t$  and the slow friction timescale  $\tau = \epsilon t$ . After writing  $\varrho_v$  and  $\phi_e$  in the mode basis, we can further expand in  $\epsilon$  as

$$r_n(t) = \sum_{k=0}^{\infty} \epsilon^k r_{kn}(t, \tau), \quad (\text{S10a})$$

$$f_n(t) = \sum_{k=0}^{\infty} \epsilon^k f_{kn}(t, \tau), \quad (\text{S10b})$$

where we explicitly separate the dependence on the two timescales. Then

$$\begin{aligned} \ddot{r}_{kn}(t, \tau) &= \partial_t^2 r_{kn} + 2\epsilon \partial_t \partial_\tau r_{kn} + \epsilon^2 \partial_\tau^2 r_{kn}, \\ \ddot{f}_{kn}(t, \tau) &= \partial_t^2 f_{kn} + 2\epsilon \partial_t \partial_\tau f_{kn} + \epsilon^2 \partial_\tau^2 f_{kn}. \end{aligned}$$

At zeroth order in  $\epsilon$ , with  $D = 0$ , Eq. (S2) becomes

$$\sum_{n=1}^V \partial_t^2 r_{0n} \varrho_{vn} = - \sum_{n=1}^V \lambda_n^2 r_{0n} \varrho_{vn}.$$

The modes  $\varrho_{vn}$  are orthonormal, so the terms decouple into separate harmonic oscillators;  $f_{kn}$  can be found from  $r_{kn}$  using Eq. (S1a). The leading order solution is then

$$\begin{aligned} r_{0n}(t) &= A_{0n}(\tau) \cos(\lambda_n t - \delta_n(\tau)), \\ f_{0n}(t) &= -A_{0n}(\tau) \sin(\lambda_n t - \delta_n(\tau)). \end{aligned}$$

At first order in  $\epsilon$ , with  $g(\mu, \phi_e) = (\mu - \phi_e^2)$ ,

$$\sum_{n=1}^V (\partial_t^2 r_{1n} + 2\partial_t \partial_\tau r_{0n}) \varrho_{vn} = - \sum_{n=1}^V \lambda_n^2 r_{1n} \varrho_{vn} + \sum_e \nabla_{ve} \left[ \mu - \left( \sum_{n=1}^E f_{0n} \phi_{en} \right)^2 \right] \sum_{l=1}^E f_{0l} \phi_{el}.$$

Multiplying by  $\varrho_{vm}$  and summing over  $v$ , we find

$$\partial_t^2 r_{1m} + 2\partial_t \partial_\tau r_{0m} = -\lambda_m^2 r_{1m} + \lambda_m \left[ \mu f_{0m} - \sum_e \phi_{em} \left( \sum_{n=1}^E f_{0n} \phi_{en} \right)^3 \right]. \quad (\text{S11})$$

## VI. LEADING ORDER AMPLITUDE DYNAMICS

In order for the expansion in Eqs. (S10a) and (S10b) to make sense, the magnitudes of the summands  $r_{kn}$  and  $f_{kn}$  must remain bounded. From Eq. (S11),  $r_{1m}$  is a harmonic oscillator with natural frequency  $\lambda_m$  driven by the zeroth order oscillations. It will have bounded oscillations only if the resonant terms in Eq. (S11), those that drive  $r_{1m}$  at its natural frequency, are zero. Finding the resonant terms and setting them to zero will fix the leading order mode amplitudes  $A_n(\tau)$ .

Expanding the cube in Eq. (S11) gives

$$\begin{aligned} \partial_t^2 r_{1m} + 2\partial_t \partial_\tau r_{0m} &= -\lambda_m^2 r_{1m} + \lambda_m \left[ \mu f_{0m} - \sum_e \phi_{em} \sum_{k,\ell,n=1}^E f_{0k} \phi_{ek} f_{0n} \phi_{el} f_{0n} \phi_{en} \right] \\ &= -\lambda_m^2 r_{1m} + \lambda_m \left[ \mu f_{0m} + \sum_{k,\ell,n=1}^E \left( \sum_e \phi_{em} \phi_{ek} \phi_{el} \phi_{en} \right) \right. \\ &\quad \left. \times A_{0k} A_{0\ell} A_{0n} \sin(\lambda_k t - \delta_k) \sin(\lambda_\ell t - \delta_\ell) \sin(\lambda_n t - \delta_n) \right]. \quad (\text{S12}) \end{aligned}$$



Now, the product of sines can be expanded into

$$\begin{aligned} \sin(\lambda_k t - \delta_k) \sin(\lambda_\ell t - \delta_\ell) \sin(\lambda_n t - \delta_n) = \frac{1}{4} & \left[ \sin(\delta_k - \delta_\ell - \delta_n - \lambda_k t + \lambda_n t + \lambda_\ell t) \right. \\ & - \sin(\delta_k - \delta_\ell + \delta_n - \lambda_k t - \lambda_n t + \lambda_\ell t) \\ & - \sin(\delta_k + \delta_\ell - \delta_n - \lambda_k t + \lambda_n t - \lambda_\ell t) \\ & \left. + \sin(\delta_k + \delta_\ell + \delta_n - \lambda_k t - \lambda_n t - \lambda_\ell t) \right]. \end{aligned}$$

We seek only resonant terms, which only occur when  $\pm\lambda_k$ ,  $\pm\lambda_\ell$ , and  $\pm\lambda_n$  sum to  $\lambda_m$ . This happens most often in one of two ways. First, we might have  $k = \ell$  and  $n = m$  or similar. Alternatively, we might have degenerate modes,  $\lambda_k = \lambda_\ell$  and  $\lambda_n = \lambda_m$ . However, we ignore the latter possibility because degeneracies add significant analytic complications, including nontrivial dynamics of their relative phases. We also ignore the rare possibility of resonant terms arising from interactions of modes with three or four distinct singular values. The results we get with these assumptions closely match simulated time series (Fig. 3e-g), suggesting that the existence of degeneracies has little impact on the dynamics of nondegenerate modes.

The remaining resonant terms in Eq. (S12) must cancel so that  $r_{1m}$  is not an oscillator of frequency  $\lambda_m$  driven at frequency  $\lambda_m$ . Thus,

$$2\partial_t \partial_\tau r_{0m} = \lambda_m \left[ \mu f_{0m} + \frac{1}{4} \left( \sum_e \phi_{em}^4 \right) A_{0m}^3 (3 \sin(\lambda_m t - \delta_m)) + 3 \sum_{k=1, k \neq m}^E \left( \sum_e \phi_{em}^2 \phi_{ek}^2 \right) A_{0k}^2 A_{0m} \frac{1}{4} (2 \sin(\lambda_m t - \delta_m)) \right].$$

Substituting in  $r_{0m}$  and  $f_{0m}$ ,

$$\begin{aligned} -2A'_{0m} \lambda_m \sin(\lambda_m t - \delta_m) + 2\lambda_m^2 \cos(\lambda_m t - \delta_m) \delta'_m = \\ \lambda_m \left[ -\mu A_{0m} \sin(\lambda_m t - \delta_m) + \frac{1}{4} \left( \sum_e \phi_{em}^4 \right) A_{0m}^3 (3 \sin(\lambda_m t - \delta_m)) + 3 \sum_{k=1, k \neq m}^E \left( \sum_e \phi_{em}^2 \phi_{ek}^2 \right) A_{0k}^2 A_{0m} \frac{1}{4} (2 \sin(\lambda_m t - \delta_m)) \right], \end{aligned}$$

where primes denote differentiation with respect to  $\tau$ . For this to hold for all  $t$  we need the coefficients of the sine and cosine terms to separately cancel. From the cosine term,  $\delta'_m = 0$ ; from the sine term,

$$A'_{0m} = \frac{1}{2} A_{0m} \left( \mu - \frac{3}{4} \left( \sum_e \phi_{em}^4 \right) A_{0m}^2 - \frac{3}{2} \sum_{k=1, k \neq m}^E \left( \sum_e \phi_{em}^2 \phi_{ek}^2 \right) A_{0k}^2 \right) \equiv \frac{1}{2} A_{0m} \left( \mu - \sum_{k=1}^E P_{mk} A_{0k}^2 \right),$$

where the matrix  $\mathbf{P}$  has entries  $P_{mk} = \frac{3}{2} (1 - \frac{1}{2} \delta_{mk}) \sum_e \phi_{em}^2 \phi_{ek}^2$ . Rewriting in terms of the squared amplitudes,

$$\frac{d}{d\tau} (A_{0m}^2) = 2A_{0m} A'_{0m} = A_{0m}^2 \left( \mu - \sum_{k=1}^E P_{mk} A_{0k}^2 \right). \quad (\text{S13})$$

As a matrix equation, with  $x_m = A_{0m}^2$ , this reads

$$\mathbf{x}' = \mathbf{x} \odot (\mu \mathbf{1} - \mathbf{P} \mathbf{x}), \quad (\text{S14})$$

where  $\mathbf{1}$  denotes the vector of ones and  $\odot$  is the component-wise product.

To find stationary points, we set  $\mathbf{x} \odot (\mu \mathbf{1} - \mathbf{P} \mathbf{x}) = 0$ . The obvious way to solve Eq. (S14) for all stationary points is to exhaustively search over combinations of active modes: on picking certain elements of  $\mathbf{x}$  to be zero, the remaining nonzero entries  $\hat{\mathbf{x}}$  are found by solving  $\hat{\mathbf{P}} \hat{\mathbf{x}} = \mu \mathbf{1}$ , where  $\hat{\mathbf{P}}$  is  $\mathbf{P}$  restricted to those modes chosen to be nonzero. Stability of a fixed point  $\mathbf{x}_0$  then follows by standard perturbation analysis: inserting a small perturbation  $\mathbf{x}_0 + \delta \mathbf{x}(\tau)$  into Eq. (S14) gives

$$\delta \mathbf{x}' = \delta \mathbf{x} - \mathbf{x}_0 \odot (\mathbf{P} \delta \mathbf{x}) - (\mathbf{P} \mathbf{x}_0) \odot \delta \mathbf{x} + O(\delta \mathbf{x}^2) \equiv \mathbf{M} \delta \mathbf{x} + O(\delta \mathbf{x}^2),$$

where  $\mathbf{I}$  denotes the identity matrix, and the eigenvalues of  $\mathbf{M}$  then determine stability in the usual fashion.

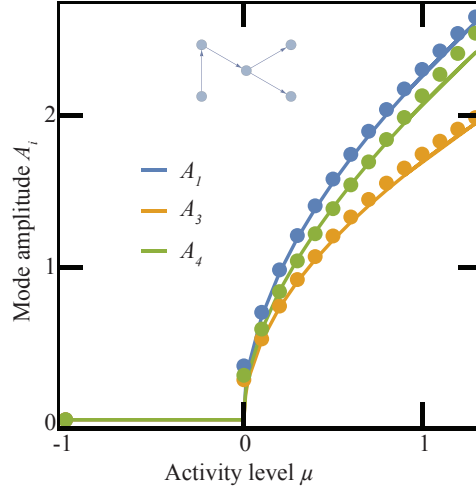


Fig. S2. Steady state amplitudes  $A_i$  as a function of activity  $\mu$  for the tree pictured undergo a Hopf bifurcation as  $\mu$  crosses 0. Dots are long-time root-mean-square amplitudes from simulations started in each mode; lines are numerical solutions of Eq. (S15). Mode  $A_2$  is too unstable to reliably observe in simulations, so it is omitted. For  $\mu < 0$ , all amplitudes go to zero in simulations; the dot included in that region is at  $\mu = -1$  where the friction is purely passive. Some deviations between simulation and analytics are expected because the simulations do not use the Rayleigh friction approximation and  $\epsilon \neq 0$ . Parameters were  $\epsilon = 0.5$  and  $D = 0$ .

## VII. ACCURACY OF RAYLEIGH FRICTION APPROXIMATION

To verify that the Rayleigh friction approximation does not significantly impact the results, we check the amplitude and stability of single modes for the full model with  $g(\mu, \phi_e) = (\mu - \phi_e^2)/(1 + \phi_e^2)$  on all edges. Here setting the first order secular terms to zero in a perturbation expansion with  $A_{0n} = A_{0p}\delta_{np}$  leads to

$$A_{0p}^2 = (\mu + 1) \sum_e \left( 2 - 2\sqrt{\frac{1}{1 + A_{0p}^2 \phi_{ep}^2}} \right). \quad (\text{S15})$$

Numerically solving Eq. (S15) for  $\mu = 1$  yields solutions within a few percent of the Rayleigh approximation solution  $1/\sqrt{P_{pp}}$  which additionally match numerical simulations of the full model even for  $\epsilon$  as large as 0.5 (Fig. S2).

When the system transitions from no energy input to active flow, the steady state amplitudes will grow with  $\mu$ . If we assume  $\mu \ll 1$  (so  $A_p \ll 1$ ) and expand the square root to order  $A_p^4$ , we find  $A_p^2 + O(A_p^4) = \mu/P_{pp}$ , exactly matching the Rayleigh friction result. The scaling  $A_p \sim \sqrt{\mu}$  is typical of a supercritical Hopf bifurcation.

## VIII. ATTRACTOR CHARACTERISTICS ON TREE NETWORKS

The mode interactions of Eq. (S14) can lead to complex oscillation patterns dependent on global, not local, topology, as shown for a 127-vertex complete binary tree in Movie 4 and Fig. S3. After initializing with zero pressure variation and flux, the system settles into quasi-steady states with dramatically different dynamics in separate regions of the tree (Fig. 3a,b). Flux in edges near the leaves of the tree tends to oscillate rapidly, driving large pressure fluctuations in nearby vertices, whereas flux oscillations near the root are comparatively slow with nearly constant pressure in the vertices (Fig. 3b,d). Since, apart from the root and leaves, each vertex has the same local topology, the different time scales emerge from the interaction of the local active friction with the global structure of the tree.

A comprehensive and precise characterization of the relative lifetimes of different attractors in large active flow networks remains out of reach with current numerical methods, in part because the range of noise levels low enough to observe state selection and high enough to observe transitions is quite small. Such a fine-tuning between thermal and active transport processes is a characteristic feature of many, if not all, biological systems that function optimally in a narrow temperature range: bacterial flagellar motors are designed to barely beat Brownian diffusion at room temperature, ATP-driven intracellular transport is tuned such that it improves moderately over thermal diffusion, and so-on. Another well-known example in this context is stochastic resonance in driven multistable systems [7]. However, as all these systems typically exhibit exponential Arrhenius-type waiting times, it is practically impossible

to completely explore their attractor statistics in the moderate-to-weak noise regime, except for the simplest two-state systems [8].

Nevertheless, long simulation runs as shown in Fig. S4 offer some insight into the qualitative behavior of attractors in active flow networks. Specifically, our simulations suggest that, while there is considerable variation in the relative occupancy of different attractors, stable states can be approximately divided in two classes: (1) states with one high energy mode at high amplitude and a few low energy modes at low amplitude and (2) states with multiple low-energy modes active at moderate amplitude, some of them degenerate. States of type (2) tend to quickly transition to other states of type (2) (Fig. S4); states of type (1) have a wide range of lifetimes but no obvious transition patterns.

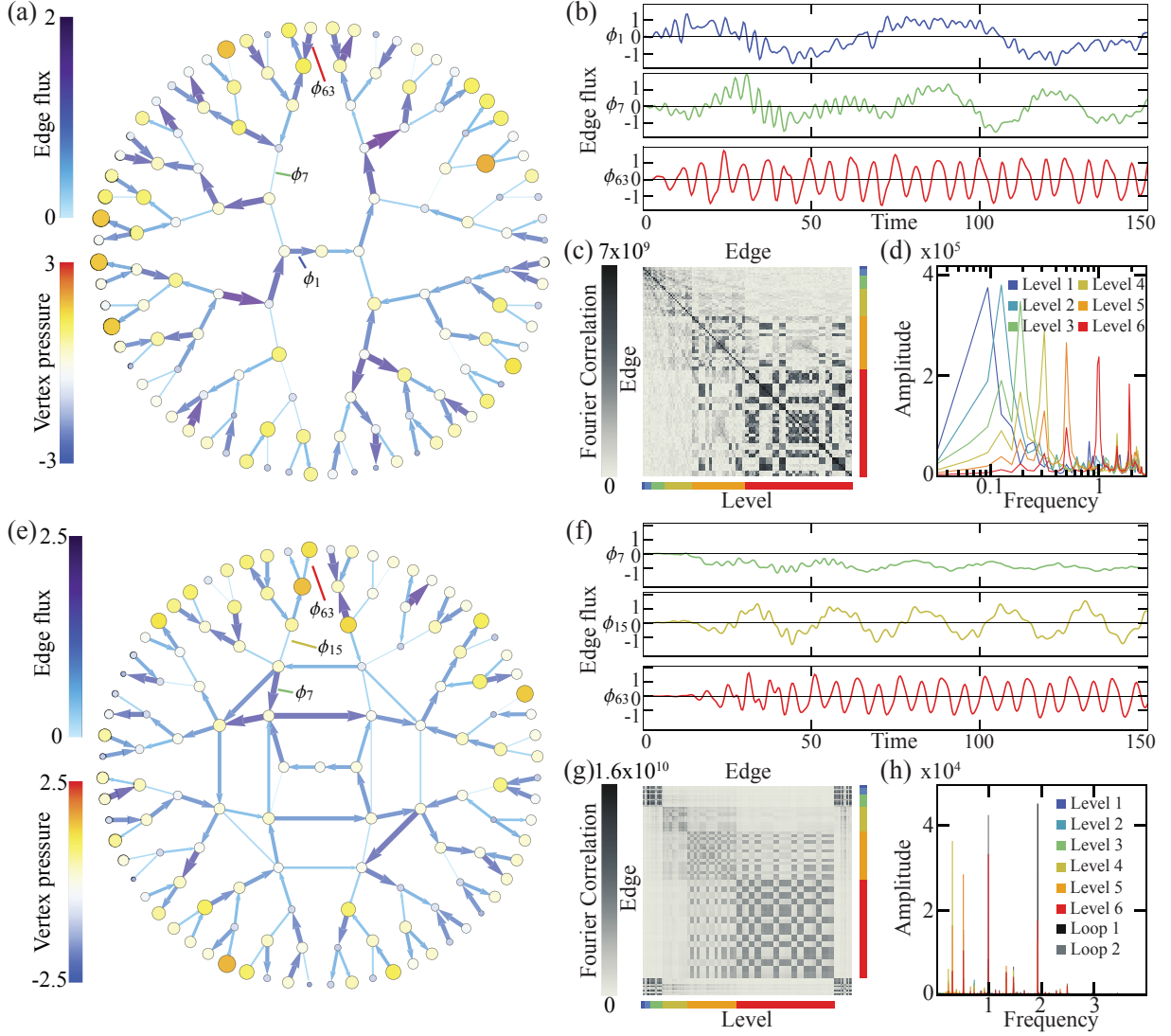


Fig. S3. Activity causes depth-dependent separation of time scales on a large tree. (a) Most pressure variation occurs near the leaves on large binary trees (Movie 4). (b) The tree in (a) develops an activity-driven steady state with slow oscillations in the center and fast oscillations near the edges, as illustrated by the flux  $\phi_e$  on the three edges labelled in (a). (c) Unnormalized correlations between the Fourier transforms of the flux through the edges of the tree in (a), with phases ignored. Colors indicate the tree level of the tail vertex of the edge. There are strong correlations within each level and between neighboring levels, but low correlations for edges in widely-separated levels. (d) Frequency spectra of each tree level, computed by taking Fourier transforms of the edge fluxes as in (c) and averaging the magnitudes across all edges at each level. A distinct primary oscillation frequency for each level can be seen, which increases with distance from the tree center. Simulation parameters in all panels are  $\epsilon = 0.5$ ,  $\mu = 1$ , and  $D = 10^{-3}$ . (e-h) While adding edges in the center leads to steady flow on cycles there, frequency still increases with distance from the center in the outer, tree-like sections.

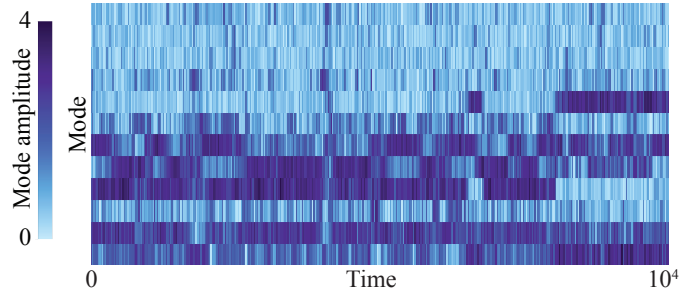


Fig. S4. Lower energy modes transition more often for the graph in Fig. 3e of the Main Text. Modes are ordered by frequency from high (top) to low (bottom). Simulation parameters are  $\epsilon = 0.5$ ,  $\mu = 1$ ,  $D = 5 \times 10^{-3}$ , identical to those in Fig. 3. Note that rows 7 and 8, the two modes that switch on and off most, are degenerate.

## IX. NETWORKS WITH CYCLES

We focus on tree networks in this paper as they allow substantial analytical progress. However, Eqs. (S1) can be applied without modification to networks with cycles. Cycles correspond to right singular vectors  $\phi_n$  of  $\nabla^\top$  with singular value zero. As these are always degenerate, we expect the conclusions of Section VI to be most accurate when there are few or no cycles. Alternatively, on a weighted graph where the edges of high conductance form a tree, the attractor characteristics will be similar to the attractors on that tree (Fig. 1; all modes pictured in Fig. S6).

Qualitatively, we find the same stochastic switching between states with subsets of modes active in simulations of Eqs. (S1) on cyclic graphs even with equal weights, with the additional feature that cyclic modes are particularly stable and take longer to transition on average (Fig. S5). For further discussion of similar dynamics on cycles, see [3].

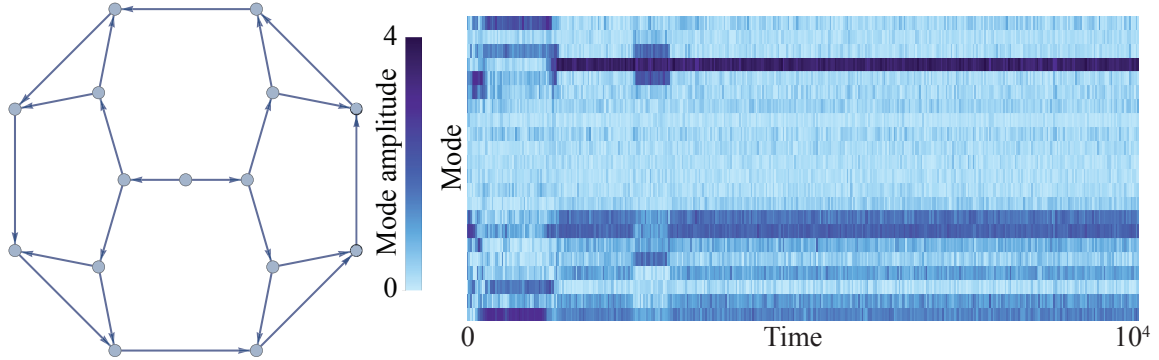


Fig. S5. States on graphs with cycles, like the one shown, tend to be more stable. Modes are ordered by frequency from high (top) to low (bottom). Note that the eight modes at the bottom, which are the only ones active in the lower half of the trace, are all cycles. Simulation parameters are  $\epsilon = 0.5$ ,  $\mu = 1$ ,  $D = 5 \times 10^{-3}$ .

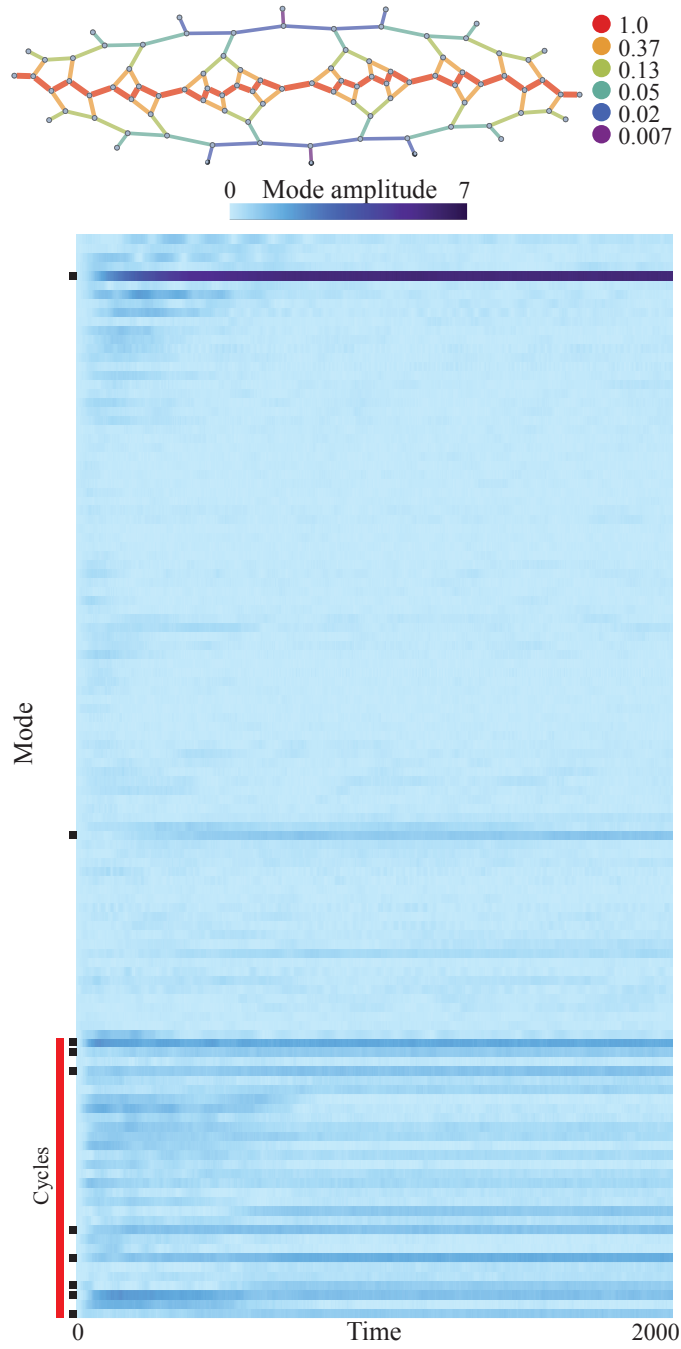


Fig. S6. Including all of the modes from the simulation in Fig. 1 of the Main Text shows clear single mode selection on this weighted network. Edges a distance  $d$  from the central red path were given weight  $e^{-d}$ . Modes are ordered by frequency from high (top) to low (bottom); the last thirty modes, marked in red, are cycles. The modes pictured in Fig. 1 are marked in black.

## X. HIGHER ORDER OSCILLATIONS

Before, by setting resonant terms to zero, we found the slow dynamics of  $A_n$ . Now we look at the non-resonant terms driving  $r_{1m}$  to find higher order effects. If we let

$$S_{i_1^{n_1} \dots i_k^{n_k}} = \sum_e \prod_{j=1}^k \phi_{ei_j}^{n_j},$$

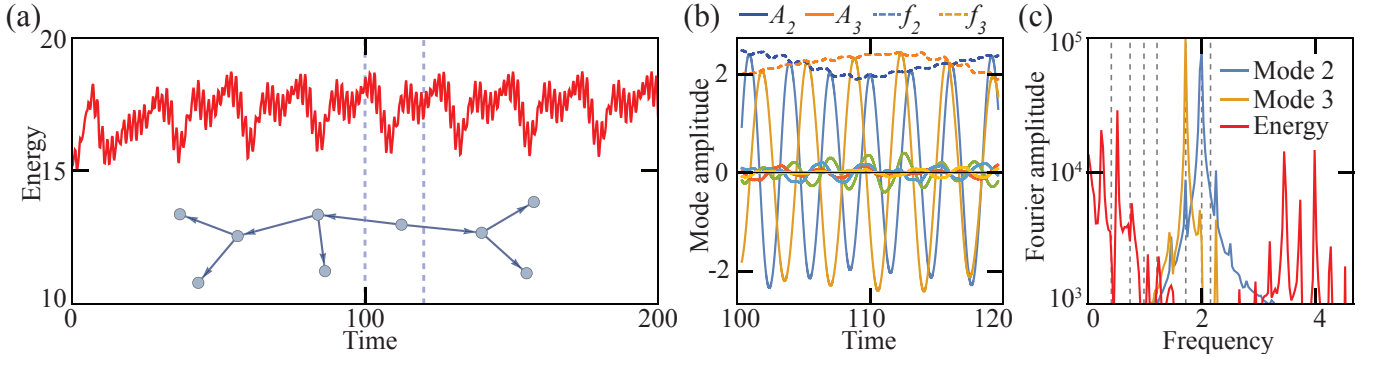


Fig. S7. Slow global oscillations emerge from the fast active dynamics. (a) First order considerations fix a constant mean flow energy; higher order effects cause significant slow oscillations about that mean. Simulation parameters were  $\mu = 1$ ,  $\epsilon = 0.5$ , and  $D = 0$ ; the tree used is inset. (b) The mode amplitudes  $A_2$  and  $A_3$ , like the energy, oscillate much more slowly than the harmonic oscillations of  $f_2$  and  $f_3$ . All other mode amplitudes (unlabelled traces) are close to zero. (c) Frequency spectra of the two active modes and the energy  $H$  for the simulation in (a) and (b). The energy oscillates due to higher-order interactions between modes at frequencies that are linear combinations of active mode frequencies, not the harmonic frequencies alone (dashed lines).

assume the resonant terms are zero, and assume  $A_{0m} = A_{0p}\delta_{mp} + A_{0q}\delta_{mq}$ , the remainder of Eq. (S11) is

$$\begin{aligned} \partial_t^2 r_{1m} + \lambda_m^2 r_{1m} = & \frac{1}{4} \lambda_m \left\{ S_{mp^3} A_{0p}^3 \sin(3\lambda_p t) + 3S_{mq^2p} A_{0p} A_{0q}^2 [\sin((2\lambda_q - \lambda_p)t) - \sin((2\lambda_q + \lambda_p)t)] \right. \\ & + 3S_{mqp^2} A_{0p}^2 A_{0q} [\sin((2\lambda_p - \lambda_q)t) - \sin((2\lambda_p + \lambda_q)t)] \\ & \left. + S_{mq^3} A_{0q}^3 \sin(3\lambda_q t) \right\}. \end{aligned} \quad (\text{S16})$$

Setting  $m = p$  and only looking at the terms closest to resonance, we obtain

$$\partial_t^2 r_{1p} + \lambda_p^2 r_{1p} \approx \frac{1}{4} \lambda_p \left\{ 3S_{q^2p^2} A_{0p} A_{0q}^2 \sin((2\lambda_q - \lambda_p)t) + 3S_{p^3q} A_{0p}^2 A_{0q} \sin((2\lambda_p - \lambda_q)t) \right\}.$$

Thus

$$\begin{aligned} r_{1p} & \approx c_1 \cos((2\lambda_q - \lambda_p)t - \delta_1) + c_2 \cos((2\lambda_p - \lambda_q)t - \delta_2), \\ f_{1p} & \approx -c_1 \sin((2\lambda_q - \lambda_p)t - \delta_1) - c_2 \sin((2\lambda_p - \lambda_q)t - \delta_2), \end{aligned}$$

where

$$\begin{aligned} c_1 & = \frac{3}{4((2\lambda_q - \lambda_p)^2 - \lambda_p^2)} \lambda_p S_{q^2p^2} A_{0p} A_{0q}^2, \\ c_2 & = \frac{3}{4((2\lambda_p - \lambda_q)^2 - \lambda_p^2)} \lambda_p S_{qp^3} A_{0p}^2 A_{0q}. \end{aligned}$$

The energy in this mode to first order in  $\epsilon$  is

$$\begin{aligned} H_p & = \frac{\lambda_p^2}{2} ((r_{0p}^2 + \epsilon r_{1p})^2 + (f_{0p}^2 + \epsilon f_{1p})^2) + O(\epsilon^2) \\ & = \frac{\lambda_p^2}{2} \left\{ A_{0p}^2 + 2\epsilon A_{0p} [c_1 \cos((2\lambda_q - 2\lambda_p)t) + c_2 \cos((\lambda_p - \lambda_q)t)] \right\} + O(\epsilon^2), \end{aligned}$$

exhibiting an order  $\epsilon$  time dependence. The coefficients  $c_1$  and  $c_2$  are small unless  $\lambda_p \approx \lambda_q$ . If we kept the frequency  $3\lambda_p$ ,  $3\lambda_q$ ,  $2\lambda_p + \lambda_q$ , and  $2\lambda_q + \lambda_p$  terms from Eq. (S16), we would find energy oscillations with frequencies  $2\lambda_p$ ,  $2\lambda_q$ ,  $3\lambda_q - \lambda_p$ , and  $\lambda_p + \lambda_q$  (Fig. S7); those oscillations have smaller amplitudes as the driving is farther from resonance.

## XI. NOISE AND THERMALIZATION

In Eqs. (S1a) and (S1b) we add Gaussian white noise only to the flux as a physically intuitive source of random fluctuations that preserve mass conservation. However, even with purely passive friction, this does not lead to equipartition of energy as seen in thermal systems.

Written as stochastic differential equations with  $g(\mu, \phi) = -1$ , Eqs. (S1a) and (S1b) become

$$d\varrho_v = \sum_e \nabla_{ve} \phi_e dt, \quad (\text{S17a})$$

$$d\phi_e = - \sum_v \nabla_{ev}^\top \varrho_v dt - \epsilon \phi_e dt + \sqrt{2D} d\tilde{B}_e(t), \quad (\text{S17b})$$

where each  $\tilde{B}_e(t)$  is standard Brownian motion. The components of the  $E$ -dimensional Brownian motion  $\mathbf{B}(t) = (\tilde{B}_1, \dots, \tilde{B}_E(t))$  in any orthonormal basis are also standard Brownian motions, so we can rewrite the system in the mode basis as

$$dr_n = \lambda_n f_n dt, \quad (\text{S18a})$$

$$df_n = -\lambda_n r_n dt - \epsilon f_n dt + \sqrt{2D} dB_n(t). \quad (\text{S18b})$$

The associated Fokker-Planck equation for the probability distribution  $p(\mathbf{r}, \mathbf{f}, t)$  is

$$\partial_t p = \sum_n \left[ -\frac{\partial}{\partial r_n} (\lambda_n f_n p) + \frac{\partial}{\partial f_n} (\lambda_n r_n p) + \frac{\partial}{\partial f_n} (\epsilon f_n p) + D \frac{\partial^2 p}{\partial f_n^2} \right]$$

with  $p \rightarrow 0$  as  $r_n, f_n \rightarrow \infty$  and  $p$  integrating to 1. Now, without friction or noise, the dynamics are governed by the Hamiltonian

$$H = \frac{1}{2} \varrho_v \nabla_{ve} \nabla_{eu} \varrho_u + \frac{1}{2} \phi_e \nabla_{ev} \nabla_{va} \phi_a = \frac{1}{2} \sum_n \lambda_n^2 (r_n^2 + f_n^2) \equiv \sum_n H_n.$$

If  $p$  is a function of the  $H_n$  alone, the Fokker-Planck equation in steady state reduces to

$$0 = \sum_n \frac{\partial}{\partial f_n} (\epsilon f_n p) + D \frac{\partial^2 p}{\partial f_n^2},$$

which has solution

$$p(H_1, \dots, H_M) \propto \prod_{n=1}^M e^{-\frac{H_n}{kT_n}},$$

where  $kT_n = \lambda_n^2 D / \epsilon$ .

Loosely, adding noise this way couples each mode to a heat bath with a distinct temperature. The result is equipartition of amplitude, not energy: the long-time average  $\langle A_n^2 \rangle$  is independent of  $n$ . Adding weak coupling between modes by making  $\mu > -1$  does not change this.

To get equipartition of energy one could change the coupling to noise, replacing the final term in Eq. (S18b) with

$$\sqrt{2D} dB_n(t) \equiv \frac{\sqrt{2D}}{\lambda_n} dB_n(t).$$

This is only possible for  $\lambda_n \neq 0$ , which precludes cyclic modes. Equation (S1b) becomes

$$d\phi_e = - \sum_v \nabla_{ev}^\top \varrho_v dt + \epsilon g(\mu, \phi_e) \phi_e dt + \sum_n \frac{1}{\lambda_n} \phi_{en} \sqrt{2D} dB_n(t).$$

The previous analysis goes through identically, leading to  $kT_n = \lambda_n^2 D / \epsilon = D / \epsilon$ .

## XII. DIFFERENTIAL GROWTH RATES

While the  $E/4$  active modes per state that we observe is significantly reduced relative to the total number of modes available, it is still a not insignificant fraction of  $E$ . There are, however, several straightforward generalizations of our model that may lead to more strict mode selection. We discuss two possibilities in this and the subsequent section: variations in activity across the network and variations in weights of vertices or edges.

For simplicity, we introduced Eqs. (S1) with a uniform activity level  $\mu$  across the entire network. This leads to equal driving on all modes: if Eq. (S13) is initialized near zero, it can be linearized to

$$\frac{d}{d\tau} (A_{0m}^2) = \mu A_{0m}^2,$$

where all modes grow at the same rate. Mode selection occurs in this system only because of interactions between modes.

In many physical systems, however, differences in growth rate between modes are important for mode selection. For example, the Rayleigh-Plateau instability [9] causes fluid jets to break apart into droplets whose size is determined by the fastest growing unstable perturbation to the jet radius. Nonlinear mode competition akin to that in Eqs. (S1) may only act on the subset of modes that grow quickly.

We can add this effect to our model by replacing  $\mu$  in Eqs. (S1) with edge-dependent parameters  $\mu_e$ . With the quadratic driving of Eq. (S9), Eq. (S1b) becomes

$$\frac{d\phi_e}{dt} = - \sum_v \nabla_{ev}^\top \varrho_v + \epsilon (\mu_e - \phi_e^2) \phi_e + \sqrt{2D} \xi_e(t).$$

Following through the previous calculations with this change, Eq. (S11) becomes

$$\partial_t^2 r_{1m} + 2\partial_t \partial_\tau r_{0m} = -\lambda_m^2 r_{1m} + \lambda_m \left[ \sum_{e,l} \phi_{em} \mu_e f_{0l} \phi_{el} - \sum_e \phi_{em} \left( \sum_{n=1}^E f_{0n} \phi_{en} \right)^3 \right].$$

The first term inside the square brackets no longer simplifies, since the  $\phi_{en}$  are not orthonormal with the weighting  $\mu_e$ . However, if we again ignore degeneracies, the only resonant term is  $\sum_e \phi_{em}^2 \mu_e f_{0m}$  from  $l = m$ . In this case, defining  $\nu_m = \sum_e \phi_{em}^2 \mu_e$ , Eq. (S13) then reads

$$\frac{d}{d\tau} (A_{0m}^2) = A_{0m}^2 \left( \nu_m - \sum_{k=1}^E P_{mk} A_{0k}^2 \right), \quad (\text{S19})$$

where modes have distinct growth rates independent of their interactions. Alternatively, one could specify  $\nu_m$  arbitrarily in Eq. (S19), though this would require more complex changes in Eq. (S1b) coupling activity across edges.

### XIII. BAND GAPS

In addition to distinct activity levels  $\mu_e$  across edges, we can also introduce edge weights  $\gamma_e$  or vertex weights  $m_v$  that vary across the network. Changing the conductances  $\gamma_e$  and volumes  $m_v$  changes our system in two ways: first, by changing the modes to the singular vectors of  $\gamma_{ve}^*$ ; and second, by changing the coupling matrix to  $\tilde{P}_{mk} = \frac{3}{2}(1 - \frac{1}{2}\delta_{mk}) \sum_e \gamma_e^{-1} \phi_{em}^2 \phi_{ek}^2$ , which depends explicitly on the edge weights.

Such changes are known to cause qualitative changes in the physics of classical spring-mass networks, including the introduction of band gaps. In an infinite one-dimensional line of beads of equal mass  $m$  connected by springs with equal spring constant  $f$ , for example, the dispersion relation between frequency  $\omega$  and wavenumber  $q$  is

$$\omega(q) = 2\sqrt{\frac{f}{m}} \left| \sin\left(\frac{qa}{2}\right) \right|,$$

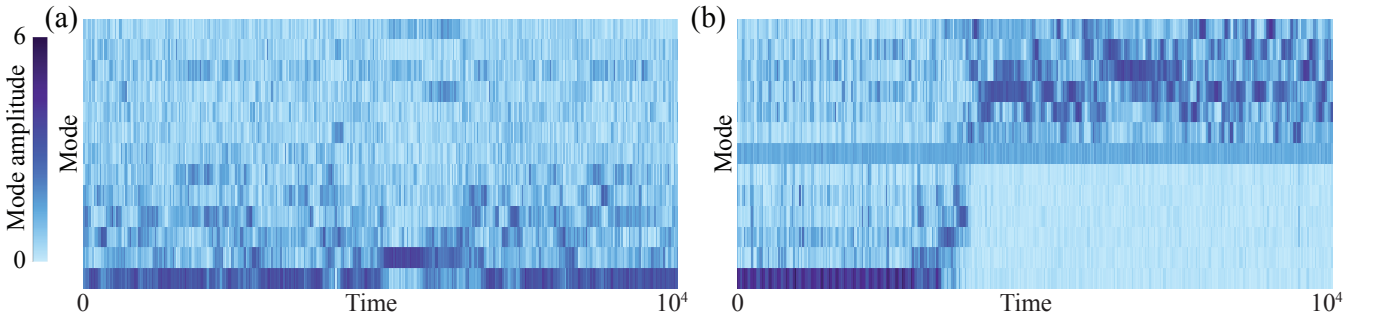


Fig. S8. The emergence of an activity-driven spectral band gap is exhibited by a simulation on a 14-vertex path with (a) all weights equal to 1 and (b) alternating vertex weights 1 and 5. Modes are ordered by frequency from high (top) to low (bottom). Note that in (b) the central  $n = 7$  mode is always active and the low energy states on the right half of the plot are significantly more suppressed than they ever are in (a). The qualitative difference is due to the presence of vertices with unequal weights, not the overall scale of the vertex weights; changing vertex weights uniformly is equivalent to rescaling other parameters. Parameters were  $\mu = 1.2$ ,  $D = 5 \times 10^{-3}$ , and  $\epsilon = 0.5$ . Both simulations used the same random seed.



where  $a$  is the size of the unit cell, in this case equal to distance between adjacent beads [10]. If instead of equal masses the beads alternate between a smaller mass  $m_1$  and larger mass  $m_2$ , the dispersion relation splits into two branches,

$$\omega(q)_\pm^2 = f \left( \frac{1}{m_1} + \frac{1}{m_2} \right) \pm f \sqrt{\left( \frac{1}{m_1} + \frac{1}{m_2} \right)^2 - \frac{4}{m_1 m_2} \sin^2 \left( \frac{qa}{2} \right)}.$$

Here a unit cell has two beads, so the distance between beads is  $a/2$ . At  $q = \pi/a$ , there is a gap between  $\omega_+ = \sqrt{2f/m_1}$  and  $\omega_- = \sqrt{2f/m_2}$ . This band gap shows up in a finite system as a large difference in frequency between modes above and below the gap.

Since varying what are effectively vertex weights causes such a clear qualitative change in behavior in the spring system, we can reasonably expect similar changes in our model. Simulations on paths with alternating vertex weights show a distinct separation of low- and high-energy states not present with uniform weights (Fig. S8), with stronger and more consistent suppression of the low-energy states and few transitions across the band gap created by nonuniform weights. Band gaps in more realistic topologies may have similar effects, allowing for enhanced control of the large-scale behavior.

- 
- [1] J. Toner, Y. Tu, and S. Ramaswamy, *Annals of Physics* **318**, 170 (2005).
  - [2] A. Souslov, B. C. van Zuiden, D. Bartolo, and V. Vitelli, arXiv:1610.06873.
  - [3] F. G. Woodhouse, A. Forrow, J. B. Fawcett, and J. Dunkel, *Proc. Natl. Acad. Sci. U.S.A.* **113**, 8200 (2016).
  - [4] M. Paoluzzi, R. Di Leonardo, and L. Angelani, *Phys. Rev. Lett.* **115**, 188303 (2015).
  - [5] F. Schweitzer, W. Ebeling, and B. Tilch, *Phys. Rev. Lett.* **80**, 5044 (1998).
  - [6] J. W. S. B. Rayleigh, *The Theory of Sound vol. 1*, 2nd ed. (Macmillan, New York, 1894) p. 81.
  - [7] L. Gammaitoni, P. Hänggi, P. Jung, and F. Marchesoni, *Rev. Mod. Phys.* **70**, 223 (1998).
  - [8] P. Hänggi, P. Talkner, and M. Borkovec, *Rev. Mod. Phys.* **62**, 251 (1990).
  - [9] J. W. S. B. Rayleigh, *Proc. Lond. Math. Soc.* **s1-10**, 4 (1878).
  - [10] P. Misra, *Physics of Condensed Matter* (Elsevier Science, Burlington, MA, 2011).